



CHORUS

This is the accepted manuscript made available via CHORUS. The article has been published as:

Nonlinear stress-strain behavior and stress-induced phase transitions in soft $\text{Pb}(\text{Zr}_{1-x}\text{Ti}_x)\text{O}_3$ at the morphotropic phase boundary

Yo-Han Seo, Daniel J. Franzbach, Jurij Koruza, Andreja Benčan, Barbara Malič, Marija Kosec, Jacob L. Jones, and Kyle G. Webber

Phys. Rev. B **87**, 094116 — Published 28 March 2013

DOI: [10.1103/PhysRevB.87.094116](https://doi.org/10.1103/PhysRevB.87.094116)

Nonlinear stress-strain behavior and stress-induced phase transitions in soft $\text{Pb}(\text{Zr}_{1-x}\text{Ti}_x)\text{O}_3$ at the morphotropic phase boundary

Yo-Han Seo¹, Daniel J. Franzbach^{1,2}, Jurij Koruza³, Andreja Benčan³, Barbara Malič³, Marija Kosec³, Jacob L. Jones⁴, Kyle G. Webber^{1,§}

¹*Institute of Materials Science, Technische Universität Darmstadt, 64287, Darmstadt, Germany*

²*Graduate School of Computational Engineering, Technische Universität Darmstadt, 64287, Darmstadt, Germany*

³*Jožef Stefan Institute, Jamova c. 39, Si-1000, Ljubljana, Slovenia*

⁴*Department of Materials Science and Engineering, University of Florida, 32611, Gainesville, FL, USA*

Abstract

Temperature-dependent stress-strain behavior of various soft PZT ($\text{Pb}_{0.98}\text{Ba}_{0.01}(\text{Zr}_{1-x}\text{Ti}_x)_{0.98}\text{Nb}_{0.02}\text{O}_3$, $0.40 < x < 0.60$) compositions was characterized between 25 and 400 °C to determine the influence of crystal structure on ferroelasticity. The ferroelastic response was found to depend significantly on the crystal phase as well as the spontaneous strain, both of which varied with temperature. The remanent strain for rhombohedral materials was shown to be above the theoretical maximum allowed by the crystal spontaneous strain. This observed behavior indicates the presence of hysteretic processes in addition to ferroelasticity during mechanical compression. A phenomenological free energy analysis was used to predict the effects of stress on the stable phase in ferroelectrics and indicates the susceptibility of the rhombohedral and tetragonal structure to a stress-induced phase transition. Modeling results indicate the relative importance of such phase transitions on macroscopic stress-strain behavior, giving an indirect method to observe field induced phase transitions in polycrystalline ferroelectrics.

1. Introduction

Ferroelectric lead zirconate titanate, $\text{Pb}(\text{Zr}_{1-x}\text{Ti}_x)\text{O}_3$ (PZT), one of the most technologically important electro-active materials, has been widely used in sensors, actuators, and ultrasonic motors because of its excellent electromechanical performance.¹⁻³ PZT, however, displays nonlinear ferroelectric and ferroelastic behavior during electrical⁴ and mechanical^{5,6} loading, respectively, resulting in hysteretic macroscopic polarization and strain loops. There have been numerous experimental investigations on the nonlinear ferroelastic stress-strain behavior of PZT-based ceramics,⁵⁻¹⁰ in addition to other ferroelastic ceramics.¹¹⁻¹⁴ It has been demonstrated that the ferroelastic behavior of PZT is influenced by the composition, dopant type and concentration, and temperature. Schäufele and Härdtl⁸ presented the stress-strain behavior of hard and soft PZT with various concentrations of PbTiO_3 . It was shown that the minimum coercive stress and maximum remanent strain for both hard and soft PZT were obtained for

compositions near the morphotropic phase boundary (MPB), which separates the ferroelectric rhombohedral and ferroelectric tetragonal phases in the composition-temperature phase diagram. This corresponds to earlier investigations that have shown similar enhancement in the electrical properties at the MPB.¹ Some investigators have attributed this to the coexistence of the tetragonal and rhombohedral phases¹⁵ or presence of an additional monoclinic Cm phase,¹⁶ while others have shown the existence of nanopolar regions in the MPB region of PZT which could result in enhanced properties.^{17,18} The reduction of domain wall energies and the resulting nanometer scale domains has been predicted by Jin *et al.*, who applied the adaptive state theory of martensites to ferroelectrics.^{19,20} As the composition is moved further from the MPB in either the tetragonal or rhombohedral direction there is a corresponding increase in the coercive stress and a decrease in the remanent strain. Cao and Evans⁵ investigated the stress-strain behaviors for both hard and soft doped PZT, showing that the coercive stress of an acceptor (hard) doped material is larger than that of a donor (soft) doped. Webber *et al.*⁹, followed by others^{10,21}, reported the temperature-dependent ferroelastic behavior of PZT ceramics in different poling states. It was shown that a reduction of the spontaneous strain is primarily responsible for a decrease of the mechanical stress-induced remanent strain with increasing temperature. In addition, there is significant change in the effective modulus during stress loading due to the anisotropic elastic properties of the perovskite crystal structure.²² Changes in the ferroelastic properties have a significant influence on the fracture behavior, which is important for various commercial applications that apply electrical, mechanical, and thermal loads on ferroelectric materials.

The concentration of $PbTiO_3$ in PZT governs the magnitude of the spontaneous lattice distortion, which is due to the internal stress by stereochemistry during cooling from the paraelectric phase.²³ The different crystallographic phases and lattice distortions are accompanied by different ferroelectric and ferroelastic responses under electrical and mechanical fields, resulting from changes in the critical energy barrier to switch domains.^{24,25} As a direct consequence of the temperature- and composition-dependence of the crystal lattice distortion, the ferroelectric-ferroelastic behavior of PZT is both composition and temperature-dependent. This has been experimentally shown by Kungl and Hoffmann,²⁶ who presented the nonlinear ferroelectric strain behavior of various PZT compositions resulting from the piezoelectric effect and domain switching processes during electric field loading with increasing temperature.

These works, however, have not addressed the influence of external stress on the stable phase state in PZT, which is expected to have a significant influence on the macroscopic behavior. Recent simulations, for example, have predicted that MPB composition of PZT display an electric field-induced phase transition at electric fields below the dielectric breakdown strength, indicating the possibility that they contribute to macroscopic behavior.²⁷ This is supported by *in situ* diffraction work that has observed such phase transitions.²⁸ Unfortunately, despite previous theoretical and experimental work, the influence of field induced phase transitions on macroscopic behavior in polycrystalline PZT is not known. In particular, there has

been to date little experimental or theoretical work on the influence of stress on the phase in PZT. In the present work, the non-linear ferroelastic behavior of soft PZT ceramics with different compositions were experimentally measured at temperatures between 25 and 400 °C. Ferroelastic hysteresis is discussed in conjunction with temperature-dependent X-ray diffraction (XRD) measurements in terms of phase and lattice distortion. Interesting results for rhombohedral compositions were observed that indicate contributions of hysteretic processes other than ferroelasticity. A phenomenological thermodynamic analysis is presented that can predict the influence of stress on the stable phase in PZT, allowing for the determination of stress-induced phase transitions. During calculations the spontaneous polarization was allowed to evolve in response to an applied mechanical stress, providing an indirect method of observing the effect of mechanical loading on the stable phase state in polycrystalline perovskites.

2. Experimental procedure

In this work, the ferroelastic behavior of Ba and Nb modified PZT solid solution ceramics ($\text{Pb}_{0.98}\text{Ba}_{0.01}(\text{Zr}_{1-x}\text{Ti}_x)_{0.98}\text{Nb}_{0.02}\text{O}_3$) with different PbTiO_3 content ($x = 0.40, 0.47, 0.49, 0.51, 0.53, 0.55$ and 0.60) was measured as a function of temperature. The compositions in this study are referred to by their PbTiO_3 content (mol%), e.g., PZT 40 for $x = 0.40$. The powders were prepared by mixed-oxide method using PbO (Sigma, 99.9% purity, 211907), TiO_2 (Alfa, 99.8% purity, 042681), ZrO_2 (TZ-0, Tosoh), Nb_2O_5 (Sigma, 99.9% purity, 208515) and BaCO_3 (Alfa, 99.8% purity, 014341) as precursors. Powder mixtures were homogenized in isopropyl alcohol ($\text{C}_3\text{H}_7\text{OH}$) in a planetary mill and calcined twice at 900 °C for 1 h with a heating/cooling rate of 5 °C/min and milling after each calcination step. After drying and sieving the powder mixtures were pressed into pellets and sintered at 1275 °C for 2 h with a heating/cooling rate of 5 °C/min.

X-ray powder diffraction was performed using PANalytical X'Pert PRO diffractometer ($\text{Cu } K\alpha_1/K\alpha_2$ radiation) equipped with a high temperature chamber, where the samples were heated in a controlled synthetic-air atmosphere, between room temperature (RT) and 400 °C with 50 °C temperature steps. For the XRD analysis of the sintered samples, the pellets were crushed into powders. The data were collected in the 2θ range from 15° to 80° with a step size of 0.026°/100s. The cell parameters of the PZT ceramics with different compositions were obtained from the Rietveld analysis, performed using the JANA2006 software.^{29, 30} A shift correction refinement was performed in order to obtain the correct zero position. The background was modeled using the Legendre polynomial and the peaks' profiles were refined using a pseudo-Voigt function. The chosen space groups for these refinements were $P4mm$ (SG no 99) and $R3m$ (SG no 160) for the tetragonal and rhombohedral PZT phases, respectively. In order to estimate the experimental error of the XRD analysis, diffractograms were collected from an independent batch of six samples of the same composition using the same experimental conditions. The data were refined as described above and the obtained error was later used for the estimation of the lattice distortion error.

As-sintered disk-shaped plates of PZT with a diameter of 30 mm and a thickness of 7 mm were ground to increase the parallelism of the circular surfaces. Cylindrical shaped samples with a diameter of ~ 5.8 mm and a height of ~ 6 mm were obtained by core drilling. After drilling, the samples were annealed at 600 °C for 1 h to eliminate residual stresses, which may be induced by the machining process. To characterize the ferroelastic behavior, the stress-strain curves were measured with an experimental setup described in detail elsewhere.⁹ Mechanical compressive stress up to -390 MPa with a rate of -3.7 MPa/s (loading) was applied to the preloaded specimen centered by an alumina alignment fixture. After reaching the maximum compressive stress, the sample was unloaded with the same loading rate back to the preload stress. The stress induced uniaxial displacement of the specimen was measured by a linear variable differential transformer (LVDT). The experimental error was previously determined as ±2 % for both maximum and remanent strain. The measurement temperatures in this study ranged from RT up to 400 °C. In order to ensure reproducibility, at least two ferroelastic measurements were performed for each composition and temperature.

3. Experimental Results

The XRD analysis revealed that the five compositions on the Ti rich side of the MPB, i.e., PZT 47, 49, 51, 55, and 60, are tetragonal between RT and 350 °C. At 400 °C they exhibited a cubic structure. PZT 45 was found to be rhombohedral up to and at 150 °C, tetragonal at 200 °C, 250 °C, and 300 °C, and cubic at 350 °C and above. The structural change between 150 °C and 200 °C was related to the crossing of the MPB with the increase of the temperature. The PZT 40 sample is rhombohedral between room temperature and 300 °C, and cubic at 350 °C and above. It should be noted, however, that the two compositions close to the MPB, i.e. PZT 45 and 47, may also contain a small amount of the tetragonal and rhombohedral phases, respectively. If present, the amount of the minority phases was too small to accurately determine the lattice parameters. On the basis of the XRD analysis it can be concluded that the MPB at room temperature is located between PZT 45 and 47, which is closer to the PZ-rich side of the phase diagram than found in the undoped PZT system.¹ This result is consistent with previous reports on barium doping of PZT.³¹ The cell parameters obtained from the XRD refinements were used to calculate the tetragonal (δ_T) and rhombohedral (δ_R) spontaneous lattice distortion for each composition and temperature according to the following equations:

$$\delta_T = \frac{c}{a} - 1 \quad (1)$$

$$\delta_R = \frac{d_{111}}{d_{11\bar{1}}} - 1 \quad (2)$$

where c and a are the tetragonal lattice parameters and d_{111} and $d_{11\bar{1}}$ are the rhombohedral lattice spacings.³² Figure 1 shows the tetragonal and rhombohedral lattice distortion for each composition as a function of temperature. Due to strong overlapping of the $(111)_R$ and the $(11\bar{1})_R$ peak, it was not possible to calculate the spontaneous lattice distortion of the PZT 40 sample at 250 °C and 300 °C. The error of the XRD analysis was estimated as described in the experimental procedure section. The obtained lattice distortion of PZT 40 at room temperature was 7.76×10^{-3} with a standard deviation of 6.6×10^{-5} . For compositions on the tetragonal side of the MPB, it was clearly observed that the tetragonal lattice distortion increased with increasing PbTiO_3 content. This effect was not seen in the rhombohedral compositions; no evident difference can be found in the rhombohedral distortion between PZT 40 and 45. These observations correspond very well with previous measurements.¹ All tetragonal and rhombohedral compositions also exhibit a reduction in spontaneous lattice distortion with increasing temperature.¹

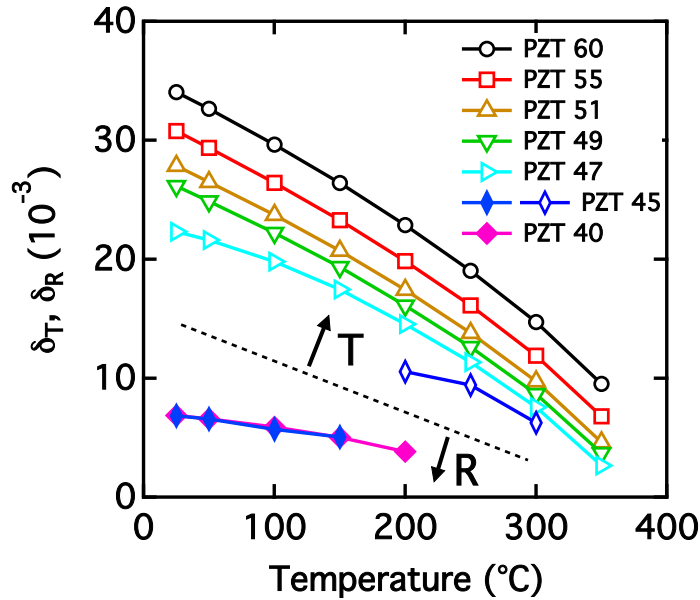


Figure 1. The tetragonal (δ_T) and rhombohedral (δ_R) lattice distortions as a function of PZT composition and temperature. Open and filled symbols represent tetragonal and rhombohedral crystal structure, respectively.

Figure 2 displays the hysteretic stress-strain curves of three representative PZT compositions at room temperature; PZT 60 composition represents the tetragonal phase, PZT 45 is the rhombohedral composition close to MPB, and PZT 40 represents a pure rhombohedral phase composition. The characterizing parameters for ferroelastic hysteresis are also illustrated; the maximum strain ϵ_{\max} is the strain induced at the maximum compressive stress level of -390 MPa, the remanent strain ϵ_r is defined as the plastic strain remaining after mechanical unloading, and the coercive stress σ_c is determined by the inflection point in the loading curve. All of these parameters depend on the crystal phase and lattice distortion, which is influenced by the

composition and temperature. It was observed that all compositions exhibited a non-linear hysteretic behavior as expected. During loading, the initial stress-strain behavior is linear elastic. With an increasing applied stress the stress-strain curve begins to deviate from the linear behavior as domains begin to ferroelastically reorient. This effect, however, saturates when the amount of switchable domains is exhausted. Therefore, the stress-strain curve again shows linear behavior at higher stress levels; a further increase in stress can no longer ferroelastically switch domains. The tetragonal PZT 60 composition shows the largest hysteresis, maximum strain, remanent strain, and coercive stress of the three compositions, in addition to the largest crystal lattice distortion. The initial slope of loading curve decreases with compositional proximity to the MPB. This is most likely because in these compositions the coercive stress is at a minimum, resulting in ferroelastic domain wall motion at reduced stresses³³ that can affect the macroscopic elastic modulus. At stresses below the coercive stress it is possible that nonlinear, plastic processes impact the determination of the material properties. In contrast, the slope of an initial unloading curve remains relatively constant between the three represented compositions.

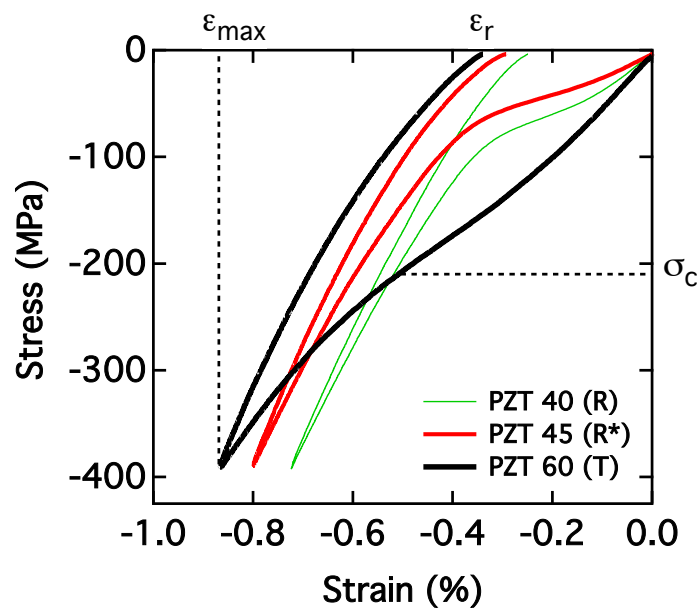


Figure 2. Stress-strain curves of three representative PZT compositions (PZT 40, 45, and 60) at room temperature. Three characteristic parameters of ferroelasticity, ϵ_{\max} , ϵ_r , and σ_c , were determined from the stress-strain curve for the PZT 60 composition. The superscript star on PZT 45 indicates the vicinity of the MPB. The star denotes that a minority tetragonal phase was found, although the fraction was too small to accurately determine.

Ferroelastic stress-strain hysteresis curves for unpoled PZT 40, 45, 47, 49, 55, and 60 specimens at 25, 200, and 400 °C are presented in Figure 3. It is apparent that with increasing temperature there is a corresponding decrease in the coercive stress, maximum strain, and remanent strain in all compositions. In addition, each composition showed a decrease in the ferroelastic hysteresis at elevated temperatures below 400 °C and linear elastic, non-hysteretic

stress-strain behavior at 400 °C. This was confirmed by XRD measurements that showed that all compositions were in the paraelectric cubic phase at 400 °C. Although, the phase transition temperature of PZT 60 lies below 400 °C, the stress-strain curve still exhibits a small hysteresis, which is may be due to a slight sample misalignment during measurement. In addition, a decrease in the initial slope of the loading curve for all compositions is observable for increasing temperature up to the Curie point. The slope of the initial unloading curve, however, appears to be temperature independent within the resolution of the measurements for the investigated temperature range.

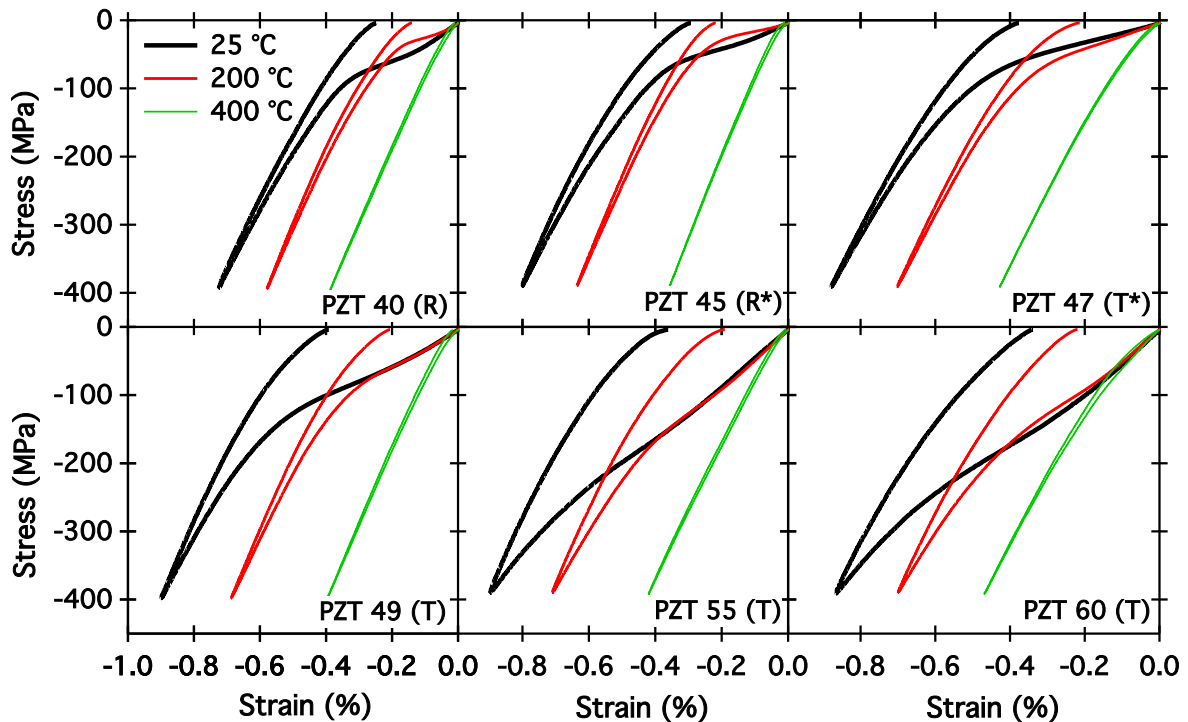


Figure 3. Stress-strain curves for six representative PZT compositions at three temperatures (25, 200, and 400 °C). A decrease in hysteresis with increasing temperature was observed for all compositions. The star denotes that a minority phase was found, although the fraction was too small to accurately determine.

4. Model Simulations and Discussion

Ferroelastic domain switching is considered to be the primary reason for the non-linear hysteretic behavior in PZT ceramics during mechanical loading above the coercive stress.^{5, 7, 8} The coercive stress is therefore an important material property to characterize the ferroelastic behavior of materials. The measured coercive stress as a function of the Ti concentration (mol%) is plotted in Figure 4 together with the compositionally dependent lattice distortions.

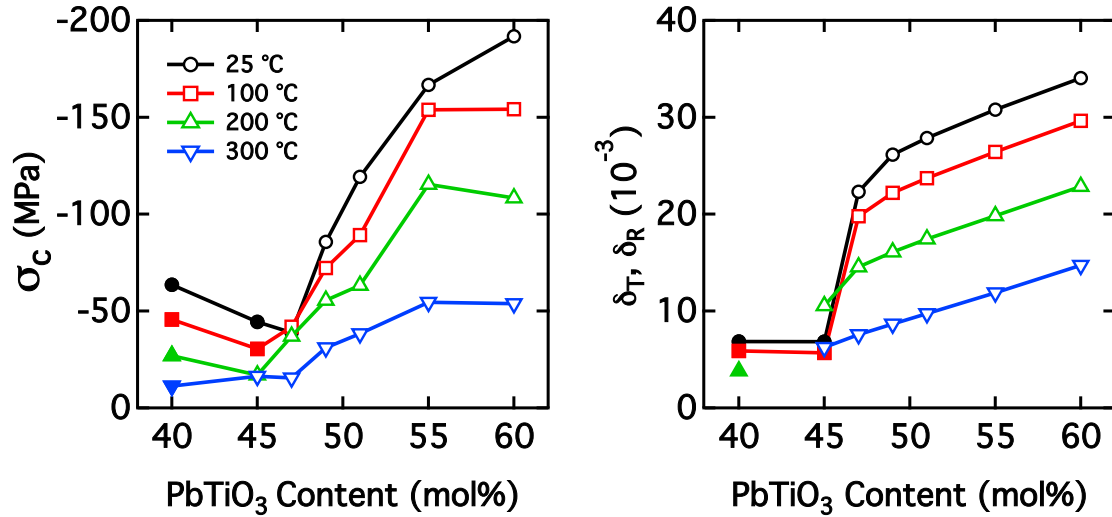


Figure 4. Coercive stress and lattice distortions as a function of PbTiO_3 content and temperature. Open and filled symbols represent tetragonal and rhombohedral crystal structure, respectively.

It was observed that an increase in the lattice distortion in the tetragonal phase (PZT 47, 49, 51, 55, and 60) is accompanied by an increase in the ferroelastic coercive stress at all measurement temperatures. It is expected that a large lattice distortion results in an increase in the internal stress, which increases the energy barrier for ferroelastic domain switching and results in a higher coercive stress.¹³ In rhombohedral compositions, however, it was found that PZT 40 had a larger coercive stress than PZT 45, despite the similar lattice distortions. This strongly indicates that, although the lattice distortion influences the energy required to ferroelastically reorient a domain, processes occurring at the MPB may also play an important role in the switching behavior. The lowest coercive stress was observed for the compositions near the MPB (PZT 45 and 47) as previously reported by Schäufele and Härdtl.⁸ Previous investigations have proposed that the coexistence of both tetragonal and rhombohedral phases in the MPB region can lead to improved properties,³⁴ although in the present case the two compositions closest to the MPB were found to have a minor phase content too small to accurately measure. Recent work by Heitmann and Rossetti has shown using a 2-4-6 Landau free energy polynomial that a minimization of the polarization anisotropy energy at the MPB is required in order to explain the PZT phase diagram.³⁵ This results in the energy barrier to polarization reorientation between ferroelectric domains becoming increasingly small at the MPB, which could be the origin of the decreased coercive stress observed here. Interestingly, the variation of coercive stress with increasing temperature in the MPB compositions (PZT 45 and 47) is low compared to other compositions further away from the MPB. For example, the coercive stress of PZT 40 and 60 at 300 °C is ~18% and 28% of the value at 25 °C, respectively, while the MPB compositions PZT 45 and 47 retain 40% and 36% of their room temperature σ_c at 300 °C, respectively.

The composition and temperature dependence of the remanent strain is apparently related to the lattice distortion of the corresponding crystal structure, as evidenced by Figure 4. The

macroscopic stress-strain behavior is typically assumed to be comprised of two contributions: an intrinsic effect (i.e., elastic compliance) and an extrinsic effect (e.g., ferroelasticity).³⁶ The strain contribution from ferroelasticity is affected by the number of domains available for switching as well as the achievable strain from each switched domain volume element, i.e., switching strain. Here, the switching strain is equivalent to the spontaneous lattice distortion, such that $\delta_r = \varepsilon_s^T$ and $\delta_R = \varepsilon_s^R$. In the following discussion, ε_s will be used to represent the switching strain for all compositions; the relevant phase is implied. Depending on the maximum stress applied, an increase in lattice strains can result in a larger remanent strain, as seen in Figures 2 and 3. If ferroelasticity is the only source of remanent strain, meaning that it is the only hysteretic process, then it is possible to predict the theoretical maximum remanent strain-to-switching strain ratio as a function of crystal phase for the saturated state. Previous researchers have calculated the theoretical maximum $\varepsilon_r/\varepsilon_s$ for the rhombohedral and the tetragonal phases for electrical and mechanical loading.^{37, 38} It was found that the maximum $\varepsilon_r/\varepsilon_s$ during compressive mechanical loading of polycrystalline samples that have an initial random orientation (i.e., untextured) was -0.269 and -0.285 for the tetragonal and rhombohedral phases, respectively. Here it was assumed that the single crystalline grains do not interact, must remain within their initial crystal phase (i.e., phase transitions were not allowed), have the same lattice distortion and retain it throughout loading, and are permitted to ferroelastically switch (i.e., no clamping effects, etc.). The larger value in rhombohedral systems (-0.285) relative to tetragonal systems (-0.269) is due to the larger number of stable spontaneous strain directions, allowing a better overall alignment with the applied mechanical stress.

Figure 5 shows the experimentally measured remanent strain normalized by the switching strain with varying PbTiO_3 content. It can be readily seen that the tetragonal phase displays $\varepsilon_r/\varepsilon_s$ ratios below the theoretical maximum. In addition, with an increasing PbTiO_3 content there was an apparent linear decrease in $\varepsilon_r/\varepsilon_s$ with increasing tetragonality. Interestingly, the $\varepsilon_r/\varepsilon_s$ ratio was not found to have a significant dependence on temperature. One possible explanation for such a phenomenon is that strong (athermal) pinning centers exist in these compositions that limit the realizable extent of ferroelastic domain wall motion. The strain ratio ($\varepsilon_r/\varepsilon_s$) used in the present work is particularly sensitive to this type of observation because it is able to subtract out the effect of changing lattice distortion (ε_s). For measurements at 25°C of tetragonal compositions, it is possible that the observed linear decrease in $\varepsilon_r/\varepsilon_s$ is due to a reduction in the number of domains that could be ferroelastically reoriented with increasing PbTiO_3 content for a maximum stress of -390 MPa. As seen in Figure 4, an increase in lattice distortion corresponds to an increase in the ferroelastic coercive stress. At the MPB the maximum stress σ_{max} was approximately 8 times larger than σ_c at 25°C , while in PZT 60 the maximum stress was only two times larger, which might not be enough to achieve a mechanically saturated state. Therefore, it is expected that the MPB compositions were in an exhausted saturated state relative to the PZT 60 composition. Previous *ex situ* XRD measurements of MPB PZT specimens mechanically compressed to -385 MPa have revealed that mechanical loading at elevated temperatures does

not significantly strengthen the domain texture relative to lower temperatures, indicating that additional domains are not ferroelastically reoriented with a decreased coercive stress at the MPB.³⁹ At elevated temperatures, however, there was a considerable decrease in the coercive stress for tetragonal compositions outside of the MPB region (Fig. 4). In the case of PZT 60, the coercive stress decreased from ~ 190 MPa at 25 °C to ~ 50 MPa at 300 °C. It is expected that a decrease in coercive stress with increasing temperature would lead to an increase in ϵ_r/ϵ_s , if the lack of a saturated domain state were the primary cause of the linear decrease in ϵ_r/ϵ_s at higher PbTiO_3 content. This was not the case. In fact, a slight decrease in ϵ_r/ϵ_s was observed with increasing temperature.

Remarkably, the values of ϵ_r/ϵ_s for the rhombohedral compositions lie significantly above the theoretical maximum, well above the measurement uncertainty, which was estimated to be $\pm 3\%$ from the XRD and ferroelastic measurements. As can be observed, PZT 45, which was shown by XRD to lie on the rhombohedral side of the MPB, displays an ϵ_r/ϵ_s ratio 50% larger than the theoretical value. With a decreasing PbTiO_3 content there was an apparent decrease in ϵ_r/ϵ_s for PZT 40, although the observed values were still found to be significantly larger than the theoretically predicted maximum. In addition, PZT 45 displayed a significant change in ϵ_r/ϵ_s between 100 and 200 °C. This was due to a structural phase transition from the rhombohedral to the tetragonal phase upon crossing the MPB during heating, supported by XRD measurements.

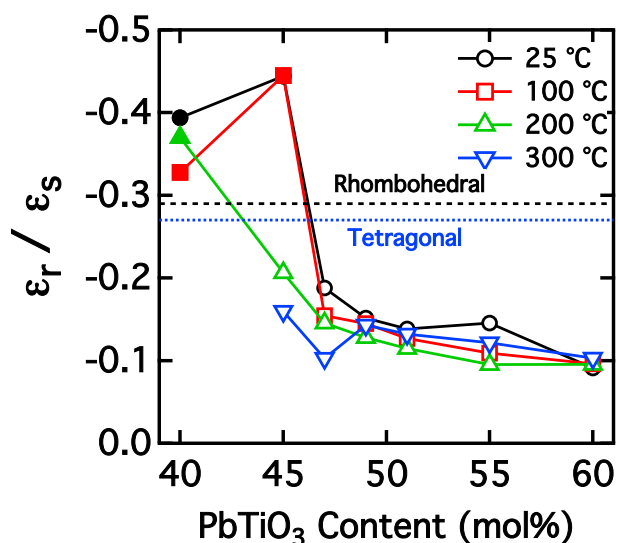


Figure 5. Macroscopic remanent strain normalized by the microscopic switching strain (ϵ_r/ϵ_s) as a function of PbTiO_3 content. Open and filled symbols represent tetragonal and rhombohedral crystal structure, respectively. The dotted blue and the dashed black horizontal lines indicate the maximum theoretical ϵ_r/ϵ_s value for the tetragonal and rhombohedral phases, assuming only ferroelasticity. Data points indicate the average measured value for each temperature and composition; error was estimated to be $\pm 3\%$.

The experimental observations presented in Figure 5 indicate the presence of additional hysteretic processes that are capable of increasing the amount of plastic strain generated during compressive loading. A possible explanation is a change of the lattice parameters after the application of a stress. This phenomenon has been previously observed during mechanical compressive loading in PZT with *in situ* X-ray⁴⁰ and neutron diffraction.⁴¹ Following mechanical loading, the interactions between neighboring grains result in a strain incompatibility that can generate local residual stresses. Hall *et al.*^{42,43} have shown that this effect is present in both rhombohedral and tetragonal structured PZT compositions during electrical loading, although the magnitude of the local stress fields depends strongly on the anisotropy of the elastic coefficients of each phase. In addition, Jones *et al.*⁴¹ have estimated the overall contribution of non-ferroelastic remanent strain contributions to account for approximately 25% of the overall macroscopic remanent strain in a purely tetragonal PZT composition. In the present work, however, only the rhombohedral compositions display an ϵ_r/ϵ_s ratio significantly larger than the theoretical maximum allowed by ferroelasticity alone. It seems likely that this drastic increase would be observed in all compositions if the irreversible changes in the lattice parameters were the primary cause. In order for the stress-induced lattice parameter changes to fully account for the increase of the ϵ_r/ϵ_s ratio above the theoretical maximum, this phenomenon would need to be nearly 58% as large as the ferroelastic contribution. It is important to note that an implied assumption here is that all of the domains can ferroelastically switch, which is not physically achievable. Reducing the ferroelastic contribution would necessitate an increase in the remanent lattice strain contribution. As shown by Jones *et al.*,⁴¹ the remanent lattice strain contribution is only 36% as large as the ferroelastic effect, considerably smaller than required to account for the experimental observations. In addition, PZT 45, which was found to transform from rhombohedral to tetragonal during heating (Fig. 1), displayed a significant decrease in ϵ_r/ϵ_s following the phase transition to tetragonal. This strongly indicates that the effect is directly linked to the rhombohedral phase and cannot solely be explained through stress-dependent hysteretic changes in the spontaneous strain.

An additional possibility is that stress induces a structural phase transition that could lead to an increase in ϵ_r/ϵ_s for PZT 40 and 45. This is in agreement with recent *in situ* synchrotron diffraction measurements, which have revealed that PZT (PIC 151) undergoes an electric field-induced phase transition that is partially irreversible.²⁸ Unfortunately, PZT single crystals of a sufficient size are not readily available to measure macroscopic field induced phase transition behavior. Therefore, a Landau free energy analysis has been utilized to determine the single domain phase transition behavior of PZT, along with the ferroelectric properties for the rhombohedral and tetragonal phases.^{27, 44} The free energy density of a single ferroelectric domain along the spontaneous polarization axis can be expanded in terms of polarization P :⁴⁵

$$G(P; \sigma) = \frac{1}{2} \alpha P^2 + \frac{1}{4} \gamma P^4 + \frac{1}{6} \delta P^6 - \frac{1}{2} s \sigma^2 - Q \sigma P^2 \quad (3)$$

where α , γ and δ are the reciprocal dielectric susceptibility and the higher-order dielectric stiffnesses at constant stress, s is the elastic compliance tensor at constant polarization, σ is the external stress, and Q are the cubic electrostrictive coefficients.⁴⁶ The evolution of the polarization of the ferroelectric domain can be determined in response to an external mechanical load by expanding Equation (3) to account for the proper crystal symmetry in three dimensions⁴⁷ and enforcing the following equilibrium conditions:

$$\left. \frac{\partial G(P; \sigma)}{\partial P} \right|_{\sigma} = 0 \quad \text{and} \quad \left. \frac{\partial^2 G(P; \sigma)}{\partial P^2} \right|_{\sigma} > 0 \quad (4)$$

The polarization evolution can be described by a Ginzburg-Landau type equation

$$\frac{\partial P}{\partial t} = -M \frac{\delta G(P; \sigma)}{\delta P} \quad (5)$$

where M is a fitting parameter describing the process mobility. Previous works have employed a similar technique to determine the electric field-^{27, 44} and hydrostatic stress-dependent⁴⁸ evolution of polarization in perovskite ferroelectrics. Haun *et al.*⁴⁹ have provided approximations of the Landau coefficients up to the 6th order for numerous PZT compositions. Implementing these coefficients into the three-dimensional expansion of Equation (3) allows for the determination of the change in polarization of a single domain of PZT in all crystallographic orientations in response to an arbitrary external field, such as electric field or stress. By minimizing the free energy function in Equation (3) for all orientations, the stable polarization directions can be readily found, as shown in Figure 6 for four PZT compositions across the MPB. Here, both the shape and the color indicate the free energy, with blue and red being the energetic minimum and maximum, respectively. In PZT 40, which is purely rhombohedral, it can be clearly seen that the energetic minima, denoted by the blue indents, lie along the $\langle 111 \rangle_c$ orientations in the unstressed state (Fig. 6, top row), while the PZT 60 composition, which is purely tetragonal, clearly shows energetic minima along the $\langle 001 \rangle_c$ orientations. Interestingly, the two compositions between these two extrema, PZT 45 and 55, display the evolution of energy landscape, where the stable polarization direction, i.e., energetic minimum, evolves from the $\langle 111 \rangle_c$ to the $\langle 001 \rangle_c$ orientation with increasing PbTiO_3 content. In all presented compositions it is apparent that both the tetragonal and the rhombohedral phases are stable, with the one being the global minimum (stable configuration) and the other the local minimum (metastable configuration).

The energy landscape distorts during the application of an external field, resulting in an evolution of the energetic minimum, i.e., an evolution of the spontaneous polarization. For illustration purposes, the energy landscapes for all four compositions are shown with a

compressive stress of -200 MPa along the $\langle 001 \rangle_c$ crystallographic direction. As expected, the polarization directions parallel to the stress for each composition were found to be in a higher energy state than those perpendicular, which would result in the evolution of the stable polarization axis during mechanical loading. Interestingly, in the case of PZT 45, the globally stable polarization direction, which was originally along the $\langle 111 \rangle_c$ orientation, was found to migrate to the $\langle 100 \rangle_c$ orientation perpendicular to the applied stress, indicating a simulated stress-induced R \rightarrow T phase transition. When the external stress is simulated in arbitrary off-axis directions, the free energy landscape will distort accordingly and allow for complex polarization evolution paths that may result in ferroelastic switching or phase transitions. Following unloading, the polarization axis in the model will be located along a principal crystallographic direction (for PZT this means $\langle 001 \rangle_c$ or $\langle 111 \rangle_c$), which may be either the globally or locally stable depending on the rotation path and applied local stress field.

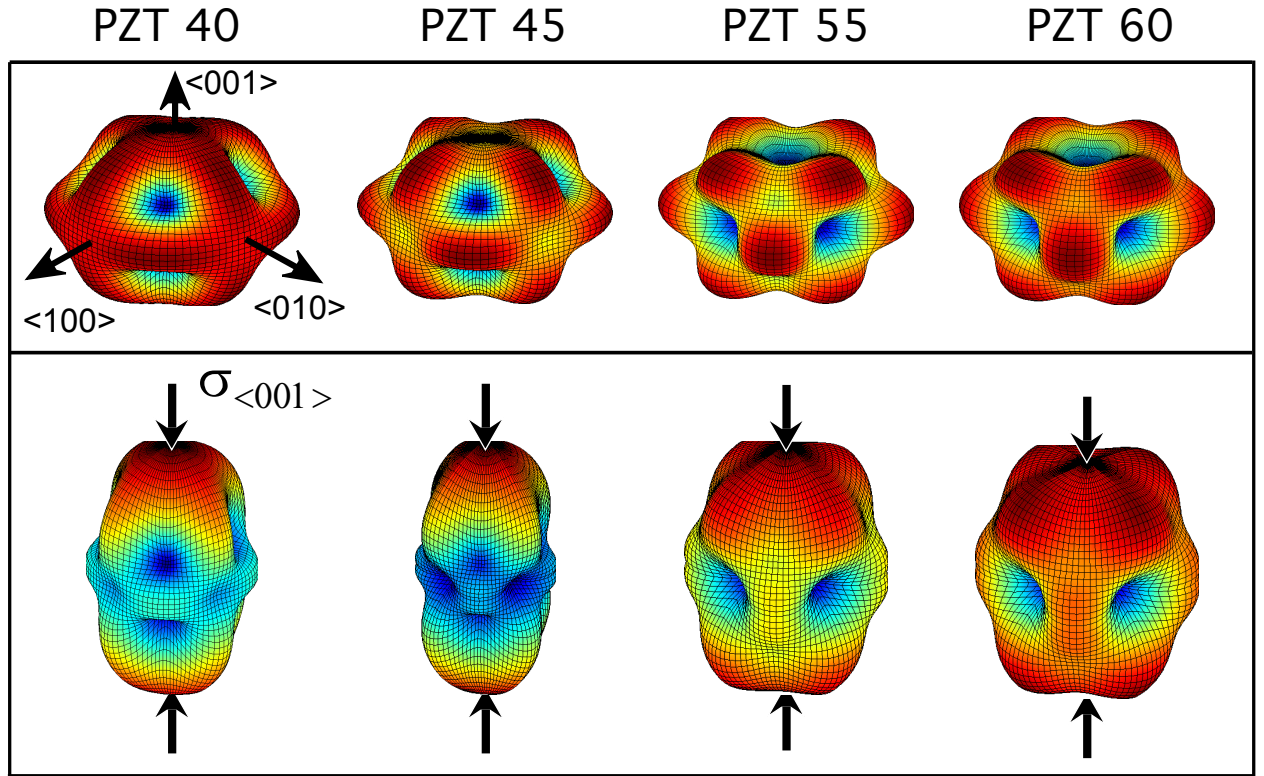


Figure 6. Three-dimensional energy landscape for PZT 40, 45, 55, and 60 in the unstressed state and with an applied compressive stress ($\sigma_{\langle 001 \rangle} = -200$ MPa) along the $\langle 001 \rangle_c$ direction. The crystallographic axes are shown for the unstressed PZT 40 and apply to all figures.

The electrostrictive coefficients Q_{11} and Q_{12} at room temperature can be determined by knowing the spontaneous strain ϵ_0 and the spontaneous polarization P_0 :

$$Q = \frac{\epsilon_0}{P_0^2} \quad (6)$$

where the spontaneous strain can be related to the switching strain with the following relation:

$$(\varepsilon_0)_{ij} = (3\delta_{3i}\delta_{3j} - \delta_{ij}) \left(\frac{\varepsilon_s}{\varepsilon_s + 3} \right) \quad (7)$$

Here, δ is Kronecker's delta. Combining Equations (6) and (7) results in expressions for the electrostrictive coefficients Q_{11} and Q_{12}

$$Q_{11} = \frac{1}{P_0^2} \left(\frac{2\varepsilon_s}{\varepsilon_s + 3} \right) \quad (8a)$$

$$Q_{12} = -\frac{\eta}{P_0^2} \left(\frac{2\varepsilon_s}{\varepsilon_s + 3} \right) \quad (8b)$$

where η is a parameter used to relate the magnitude of the Q_{11} to Q_{12} . As previously shown, the application of a hydrostatic stress can shift the Curie temperature of a perovskite ferroelectric,^{50,51} which is only possible when $Q_{11} > |2Q_{12}|$. Previous work has indicated that $\eta \approx 0.30 - 0.48$ for various perovskite ferroelectrics.^{51,52} In particular, Haun et al. has provided estimates of Q_{11} and Q_{12} for PZT as a function of PbTiO_3 content,⁴⁹ where η varied from approximately 0.30 to 0.48, depending on composition. In the vicinity of the MPB, however, Haun et al. found that $\eta = 0.48$. Due to the limited and varying data available, it was assumed during simulations that $\eta = 0.45$ for all compositions and phases. As a consequence of the changing spontaneous strain and polarization values between the rhombohedral and tetragonal phases, the electrostrictive coefficients for each phase are different. The electrostrictive coefficients Q_{11} and Q_{12} at room temperature for each phase can be determined by combining data from experimental measurements and calculations. The spontaneous polarization P_0 of the rhombohedral and tetragonal phase for a PbTiO_3 content between 40 and 60 mol% was calculated using Equation (5) for a stress-free condition (Fig. 7a), in reasonable agreement with previous estimates for MPB compositions of PZT.⁵³ The Landau coefficients for each composition were determined by linearly interpolating between the values provided by Haun et al.⁴⁹ Interestingly, it was found that both phases were stable in the stress-free state, regardless of the composition. However, while both phases were stable, only one represented the global energetic minimum. In higher PbTiO_3 compositions the global minimum lies along the $\langle 100 \rangle_c$ directions, while in lower PbTiO_3 compositions the global minimum is found along the $\langle 111 \rangle_c$ directions. The minority phase was found to be metastable, representing a local minimum of the Landau energy landscape. This can be clearly seen in Figure 6, where the free energy landscape for all four compositions in the unloaded state show a local or global minimum in tetragonal and rhombohedral directions. At approximately 52 mol% PbTiO_3 , the magnitude of the spontaneous polarization reverses, indicating a change in the globally stable phase. The spontaneous strain ε_0 for each composition

was determined at room temperature with XRD analysis (Fig. 7b). Due to the peak overlap in the MPB compositions, which occurred in all groups of peaks in the investigated 2θ range between 15° and 80° at 250°C and 300°C , the spontaneous strains could not be directly measured for both phases. Therefore, the measured data was extrapolated to obtain spontaneous strain values for both phases in the PZT 40, 45, 47, and 49 compositions. Extrapolated data points are indicated as open symbols in Figure 7b. The Q_{44} coefficient, which describes the effect of shear stresses on the free energy density, can be determined through the isotropy condition^{54, 55}

$$Q_{44} = 2(Q_{11} - Q_{12}) \quad (9)$$

The complete model parameters for each material are provided in Table 1.

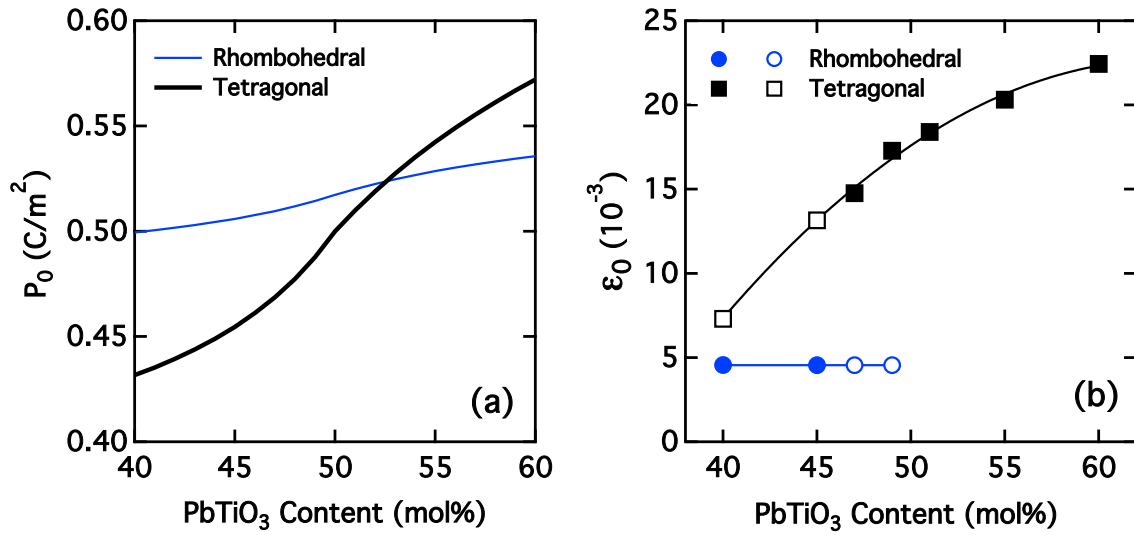


Figure 7. The calculated spontaneous polarization and the measured spontaneous strain as a function of PbTiO₃ content. The filled symbols indicate experimental measurements, while the open symbols indicate extrapolated values.

During simulations, the applied external fields in an off-axis crystallographic orientation resulted in the stable polarization direction, which follows the local energy minimum, to rotate through non-principal orientations. This has been previously shown for a tetragonal variant electrically loaded in the $[110]_c$ -orientation.⁴⁴ The polarization was predicted to rotate from the tetragonal $[100]_c$ direction to the orthorhombic $[110]_c$ direction through an intermediate phase, where the stable polarization vector does not lie along one of the principal axes.⁴⁴ In order to determine the effective electrostrictive coefficients for off-axis polarization directions, the following function, which describes the proximity of the current polar axis to the rhombohedral $\langle 111 \rangle_c$ crystallographic orientation, is proposed:

$$\xi = \frac{1}{2\|P\|^2} \sum_{i=1}^3 \sum_{j=1}^3 (1 - \delta_{ij}) |P_i P_j| \quad (10)$$

where the effective electrostrictive coefficient \tilde{Q} is the linear combination of the rhombohedral and tetragonal electrostrictive coefficients Q^R and Q^T , respectively, such that:

$$\tilde{Q} = Q_n^R \xi + Q_n^T (1 - \xi) \quad (11)$$

where the subscript n denotes the component of interest, e.g., Q_{11}^R , etc.

Table 1. The model parameters at 25 °C.

	PbTiO ₃ Content (mol%)				units
	40	45	47	49	
α_1	-7.904	-6.396	-5.792	-5.188	V m C ⁻¹
α_{11}	13.620	9.192	7.421	5.650	V m ⁵ C ⁻³
α_{12}	2.391	2.063	1.932	1.801	V m ⁵ C ⁻³
α_{111}	2.713	2.025	1.749	1.474	V m ⁹ C ⁻⁵
α_{112}	12.130	9.129	7.929	6.728	V m ⁹ C ⁻⁵
α_{123}	-5.890	-4.292	-3.733	-3.174	V m ⁹ C ⁻⁵
Q_{11}^T	0.0394	0.0637	0.0672	0.0727	m ⁴ C ⁻²
Q_{12}^T	-0.0177	-0.0286	-0.0302	-0.0327	m ⁴ C ⁻²
Q_{44}^T	0.1142	0.1846	0.1949	0.2107	m ⁴ C ⁻²
Q_{11}^R	0.0183	0.0178	0.0175	0.0172	m ⁴ C ⁻²
Q_{12}^R	-0.0082	-0.0080	-0.0079	-0.0077	m ⁴ C ⁻²
Q_{44}^R	0.0530	0.0516	0.0508	0.0498	m ⁴ C ⁻²

To this point, only single domains of ferroelectric materials have been considered. In a stressed polycrystalline material, however, there are numerous, randomly oriented single crystal grains, each with a unique local stress field that can be determined by the orientation of its crystallographic direction in relation to the global coordinate system. The effective free energy of a polycrystalline system can be determined by integrating throughout Euclidean space:

$$\tilde{G}(P; \sigma) = \int_0^\pi \int_0^{2\pi} \int_0^{2\pi} G(P; \sigma) f(\phi) f(\theta) f(\psi) d\psi d\theta d\phi \quad (12)$$

where $f(\phi)$, $f(\theta)$, and $f(\psi)$ are distribution functions defined by the Euler angles ϕ , θ , and ψ .

Equation (12) was solved numerically for 3×10^5 individual, non-interacting single domain ‘grains’, where each grain possessed a unique Euler angle set (ϕ, θ, ψ) selected to ensure an even distribution of polar axes. During calculations the mobility parameter M was chosen to be $2.5 \times 10^{-9} \text{ A V}^{-1} \text{ m}^{-1}$ with a time step size of $1 \times 10^{-3} \text{ s}$ for all compositions. This was found to be sufficiently small to allow for program convergence and smooth polarization evolution. Simulations were performed for PZT 40, 45, 47, and 49 using the material parameters in Table 1. During calculations an arbitrarily large uniaxial compressive stress of 50 GPa was utilized to ensure a saturated remanent state, which was defined as the stress above which no increase in remanent strain was found. Model results are shown in Figure 8 and compared to experimental measurements at 25 °C. Interestingly, the model is able to very accurately predict the important features of ϵ_r/ϵ_s as a function of composition; a maximum is found on the rhombohedral side of the MPB (PZT 45), with significantly decreasing values on either side. In general, the model also predicted ϵ_r/ϵ_s values in good agreement with experimental data. There was, however, an under-prediction for PZT 40. The Landau coefficients used have a significant impact on the simulation results, which is expected to be a primary cause for variations between model and experimental results. In addition, it is anticipated that local fields in the polycrystalline material also act to hinder the motion of domain walls and interphase boundaries and could lead to differences with simulations.

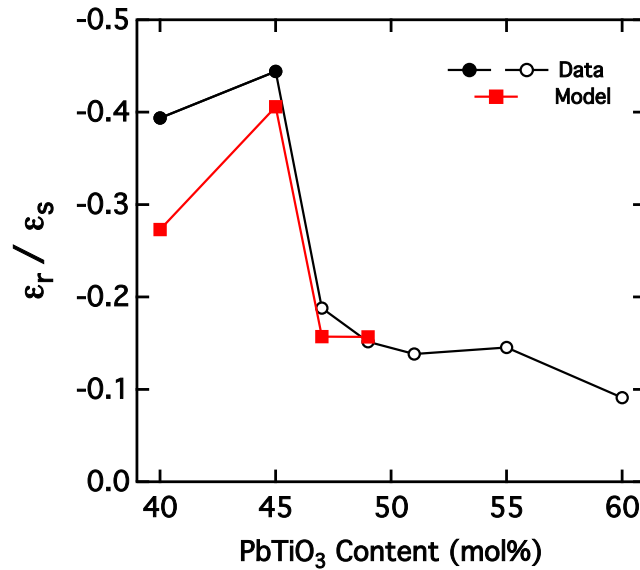


Figure 8. Comparison of experimental measurements and model results at 25 °C. Filled symbols indicate compositions that were originally rhombohedral, while open symbols were originally tetragonal.

To better understand the results, the final phase volume fraction in the remanent state was calculated from the simulation results using Equation (10), shown in Figure 9. When $\xi = 1$ the stable phase is rhombohedral, while when $\xi = 0$ the stable phase is tetragonal. ξ values between

these extremes indicate a monoclinic phase. All configurations other than tetragonal or rhombohedral were expected to be unstable in the unloaded state with a sixth order formulation of free energy density.⁵⁷ Here, however, the shape of the $\langle 111 \rangle_c$ and $\langle 001 \rangle_c$ minima also play an important role. In the case of the rhombohedral phase, the minima along the $\langle 111 \rangle_c$ -directions were found to be relatively deep, with a significant gradient. The minima along the $\langle 001 \rangle_c$ -directions, however, were flatter in nature. This can be seen in Figure 6, particularly for PZT 40. This is significant because the flatness of the minima allows the polarization direction to remain artificially stable along a non-principle crystallographic orientation. Essentially, the polarization attempts to evolve in a time-dependent manner to the $\langle 001 \rangle_c$ -orientation, which is the local minima, but loses the necessary driving force due to the drastic reduction in the free energy gradient. In the simulations it was assumed that polarization changes of less than $1 \times 10^{-13} \text{ C m}^{-2}$ between time steps indicated a stable configuration. Despite the small stability criterion, some polarization clustering around $\xi = 0$ was found for the rhombohedral compositions PZT 40 and 45. For this reason, it was assumed that the simulated grains in this region ($0 \leq \xi \leq 0.1$) belonged to the tetragonal phase. Polarization clustering was not observed in the $\langle 111 \rangle_c$ -directions; ξ values in the range $0.99 \leq \xi \leq 1$ were taken to be rhombohedral. Interestingly, the model still predicted a small non-tetragonal and non-rhombohedral volume fraction in the remanent state in PZT 40, which is again due to the shape of the $\langle 001 \rangle_c$ energy minima.

Simulation results showed that rhombohedral compositions increased in tetragonal composition by 19 to 31% for PZT 40 and PZT 45, respectively, while tetragonal compositions were predicted to increase in the rhombohedral content by 62 to 57% for PZT 47 and PZT 49, respectively. In the loaded state the rhombohedral phase was more favorable due to the smaller electrostrictive coefficients, which resulted in more phase transitions predicted for the tetragonal phase than the rhombohedral phase. It was found that the Q_{44} constant also had a significant influence on the final ϵ_r/ϵ_s ratio; at lower values R \rightarrow T transitions were more likely, which increased the saturated remanent strain obtained. Although this seems counterintuitive, it helps answer why a maximum on the rhombohedral side of the MPB is observed. When determining the ϵ_r/ϵ_s ratio for a real material, only the initial switching strain in the initial, unloaded state was taken into account. Following the simulated compression, the remanent strain in the model is a composite value comprised of ferroelastic and phase transition contributions. However, this composite remanent strain is normalized only by the initial rhombohedral switching strain; the influence of the tetragonal phase, i.e., stress-induced phase transition contribution, is not considered. Due to the larger spontaneous strain of the tetragonal phase relative to the rhombohedral phase, the ϵ_r/ϵ_s ratio can be significantly increased. The remanent strain of the tetragonal materials is also comprised of both a ferroelastic and a phase transition contribution. In this case, however, the stress-induced phase transition leads to an increase in the volume fraction of the rhombohedral phase, which has a smaller spontaneous strain than the original tetragonal phase. Even though the rhombohedral domain may be more favorably aligned to the applied compressive stress, the smaller rhombohedral spontaneous strain reduces the final

composite remanent strain and decreases the ϵ_r/ϵ_s ratio. This also explains the smaller ϵ_r/ϵ_s ratio in PZT 40 compared to PZT 45. In PZT 40 the tetragonal phase is less stable than in PZT 45, evidenced by the increased shallowness of the $\langle 001 \rangle_c$ energy wells in the unstressed state (Fig. 6). In PZT 40, this results in a reduction in the number of R→T phase transitions occurring during simulated mechanical compression (Fig. 9). In addition, the spontaneous strain of the tetragonal phase is smaller for PZT 40 than PZT 45, meaning that the contribution of each R→T phase transition to the composite remanent strain is also diminished. Both of these effects result in a smaller ϵ_r/ϵ_s ratio for PZT 40 than PZT 45.

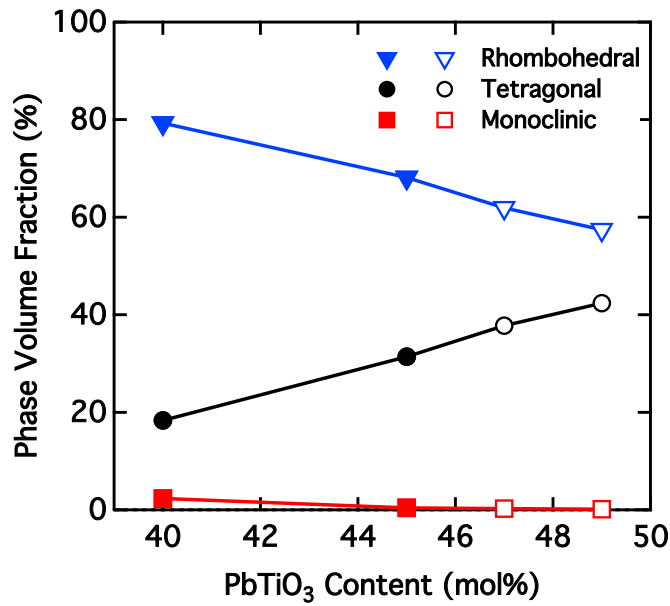


Figure 9. Predicted phase volume fraction in the saturated remanent state for PZT 40, 45, 47, and 49. Filled symbols indicate compositions that were originally rhombohedral, while open symbols were originally tetragonal.

The maximum theoretical ϵ_r/ϵ_s ratio predicted with this model for tetragonal compositions was smaller than the theoretical maximum from the ferroelasticity-only model, indicating the negative impact of T→R phase transitions on the maximum achievable remanent strain. Here, the stress-induced phase transitions and the increase in the spontaneous strain of the tetragonal phase were found to work counteractive against one another. The simulations predicted that during mechanical loading T→R phase transitions occur more readily in tetragonal compositions than R→T phase transitions in rhombohedral compositions (Fig. 9). However, even though more grains in PZT 47 transitioned from tetragonal to rhombohedral with the application of stress than in PZT 49, the increase in the tetragonality of PZT 49 increased the ferroelastic contribution to the remanent strain. In experimental measurements a linear decrease in ϵ_r/ϵ_s with increasing tetragonality was observed. Simulations, however, did not take local fields and interactions into account, allowing all domains to reorient. Local interaction effects are expected to make

significant contributions to the achievable saturated state, with some effects such as intergranular stresses increasing with PbTiO_3 content. Local, spontaneous strain-induced stresses have been shown to have a significant influence on the domain wall motion in various PZT compositions.⁵⁸ As a result, it was found that the Rayleigh parameters were significantly larger in the rhombohedral phase than in the tetragonal phase, which was attributed to local stresses originating from the increased spontaneous lattice distortions in the tetragonal phase exerting a clamping effect on the irreversible displacement of domain walls. Interestingly, however, simulations showed stress-induced phase transition behavior to the metastable phase during compressive loading in all materials. Although the predicted volume fraction of material that underwent a stress-induced phase transition seem high (particularly on the tetragonal side of the MPB), the simulations indicate that such transitions are possible and that they can help explain the extraordinary ϵ_r/ϵ_s values of the rhombohedral phase.

In real materials there are many non-linear processes, e.g., grain-to-grain interactions, defects, domain clamping, etc., that are not included in the simulations and significantly limit the number of domains that can reorient with an applied stress as well as lead to a back switching effect during unloading. The simulations, however, represent a theoretical maximum that is likely unobtainable in real materials; not all domains are free to ferroelastically switch or undergo a phase transition. Despite this, the model accurately predicted the value and the change in the ϵ_r/ϵ_s ratio as a function of composition. It was found that a small volume fraction of grains that undergo an R→T phase transition can significantly increase the experimentally measured ϵ_r/ϵ_s ratio in rhombohedral PZT. The T→R phase transitions were predicted to occur more easily than the converse R→T transitions, increasing the likelihood that the stress-induced phase transitions can be directly observed using laboratory (i.e., low-energy) X-rays where the penetration depths can cause surface measurements to significantly vary in comparison to bulk behavior.

5. Summary

The stress-strain behavior of soft PZT as a function of compositions and temperature was investigated. The remanent strain state was strongly influenced by the spontaneous switching strain, which was measured by XRD measurements for varying PZT compositions and increasing temperature. Surprisingly, the remanent-to-switching strain ratio of the rhombohedral materials was found to surpass the theoretical maximum, indicating the existence of hysteretic processes in addition to ferroelasticity. A free energy analysis was proposed that includes effects of stress-induced phase transitions between the tetragonal and rhombohedral phases. The predicted theoretical maximum remanent-to-switching strain values are in good agreement with those observed in the experimental measurements, indicating that phase transitions potentially play an important role in the ferroelastic behavior of rhombohedral PZT.

Acknowledgement

A.B., J.K., B.M., and M.K. would like to thank financial support from the European Union under the Seventh Framework project HIGH-PERformance Piezoelectric Actuators (HIPER-Act). D.J.F. acknowledges financial support from the Graduate School of Computational Engineering. Y.H.S. would like to thank financial support from the Leibniz programme of the Deutsche Forschungsgemeinschaft under RO 954/22. J.J. acknowledges support for his contributions from the U.S. NSF award DMR-0746902 and the Army Research Office through contract number W911NF-09-1-0435. K.G.W. gratefully acknowledges the support of the Deutsche Forschungsgemeinschaft under WE4972/1-1. K.G.W. would also like to thank Dr. Hans Kungl for very helpful discussions.

References

- 1 B. Jaffe, W. R. Cook, and H. Jaffe, *Piezoelectric Ceramics* (Academic Press, London, 1971).
- 2 K. Uchino, *Acta Mater* **46**, 3745 (1998).
- 3 K. Uchino, *Ferroelectric Devices* (Marcel Dekker, New York, 2000).
- 4 D. Damjanovic, *Rep. Prog. Phys.* **61**, 1267 (1998).
- 5 H. Cao and A. G. Evans, *J Am Ceram Soc* **76**, 890 (1993).
- 6 J. Y. Li, R. C. Rogan, E. Ustundag, and K. Bhattacharya, *Nat Mater* **4**, 776 (2005).
- 7 C. S. Lynch, *Acta Mater* **44**, 4137 (1996).
- 8 A. B. Schäufele and K. H. Härdtl, *J Am Ceram Soc* **79**, 2637 (1996).
- 9 K. G. Webber, E. Aulbach, T. Key, M. Marsilius, T. Granzow, and J. Rödel, *Acta Mater.* **57**, 4614 (2009).
- 10 Y. W. Li, X. L. Zhou, and F. X. Li, *J Phys D: Appl Phys* **43**, 175501 (2010).
- 11 J. S. Forrester, E. H. Kisi, and A. J. Studer, *J Eur Ceram Soc* **25**, 447 (2005).
- 12 S. Faaland, T. Grande, M.-A. Einarsrud, P. E. Vullum, and R. Holmestad, *J Am Ceram Soc* **88**, 726 (2005).
- 13 T. Leist, K. G. Webber, W. Jo, T. Granzow, E. Aulbach, J. Suffner, and J. Rödel, *J. Appl. Phys.* **109**, 054109 (2011).
- 14 T. Leist, K. G. Webber, W. Jo, E. Aulbach, J. Rödel, A. D. Prewitt, J. L. Jones, J. Schmidlin, and C. R. Hubbard, *Acta Mater.* **58**, 5962 (2010).
- 15 W. W. Cao and L. E. Cross, *Phys. Rev. B* **47**, 4825 (1993).
- 16 R. Guo, L. E. Cross, S. E. Park, B. Noheda, D. E. Cox, and G. Shirane, *Phys. Rev. Lett.* **84**, 5423 (2000).
- 17 K. A. Schoenau, L. A. Schmitt, M. Knapp, H. Fuess, R.-A. Eichel, H. Kungl, and M. J. Hoffmann, *Phys. Rev. B* **75** (2007).
- 18 R. Theissmann, L. A. Schmitt, J. Kling, R. Schierholz, K. A. Schoenau, H. Fuess, M. Knapp, H. Kungl, and M. J. Hoffmann, *J. Appl. Phys.* **102** (2007).
- 19 Y. M. Jin, Y. U. Wang, A. G. Khachatryan, J. F. Li, and D. Viehland, *Phys. Rev. Lett.* **91** (2003).
- 20 Y. M. Jin, Y. U. Wang, A. G. Khachatryan, J. F. Li, and D. Viehland, *J. Appl. Phys.* **94**, 3629 (2003).
- 21 M. Marsilius, K. G. Webber, E. Aulbach, and T. Granzow, *J Am Ceram Soc* **93**, 2850 (2011).
- 22 T. Fett, D. Munz, and G. Thun, *Ferroelectr.* **274**, 67 (2002).
- 23 A. E. Glazounov, H. Kungl, J. T. Reszat, M. J. Hoffmann, A. Kolleck, G. A. Schneider, and T. Wroblewski, *J. Am. Ceram. Soc.* **84**, 2921 (2001).
- 24 M. J. Hoffmann, M. Hammer, A. Endriss, and D. C. Lupascu, *Acta Mater* **49**, 1301 (2001).

25 M. J. Hoffmann and H. Kungl, *Curr Opin Solid ST M* **8**, 51 (2004).
26 H. Kungl and M. J. Hoffmann, *Acta Mater.* **55**, 5780 (2007).
27 A. J. Bell, *Appl. Phys. Lett.* **76**, 109 (2000).
28 M. Hinterstein, J. Rouquette, J. Haines, P. Papet, M. Knapp, J. Glaum, and H. Fuess,
29 *Phys. Rev. Lett.* **107** (2011).
30 V. Petricek and M. Dusek, *The Crystallographic Computing System JANA 2006* (Institute
31 of Physics, Academy of Sciences of the Czech Republic, Praha, 2006).
32 H. M. Rietveld, *J Appl Crystallogr* **2**, 65 (1969).
33 K. Ramam and M. Lopez, *J Phys D: Appl Phys* **39**, 4466 (2006).
34 N. Uchida and T. Ikeda, *Jpn J Appl Phys* **6**, 1079 (1967).
35 J. Muñoz-Saldaña, G. A. Schneider, and L. M. Eng, *Surface Science Letters* **480**, L402
36 (2001).
37 G. A. Rossetti Jr., W. Zhang, and A. G. Khachaturyan, *Appl. Phys. Lett.* **88**, 072912
38 (2006).
39 A. A. Heitmann and G. A. Rossetti, Jr., *Philos. Mag.* **90**, 71 (2010).
40 A. Pramanick, D. Damjanovic, J. E. Daniels, J. C. Nino, and J. L. Jones, *J. Am. Ceram.*
41 *Soc.* **94**, 293 (2011).
42 J. L. Jones, M. Hoffman, and K. J. Bowman, *J. Appl. Phys.* **98**, 024115 (2005).
43 F. X. Li, D. N. Fang, and A. K. Soh, *Scripta Mater.* **54**, 1241 (2006).
44 K. G. Webber, E. Aulbach, T. Key, M. Marsilius, T. Granzow, and J. Rödel, *Acta Mater*
45 **57**, 4614 (2009).
46 D. A. Hall, A. Steuwer, B. Cherdhirunkorn, P. J. Withers, and T. Mori, *Mater. Sci. Eng.,*
47 *A* **409**, 206 (2005).
48 J. L. Jones, M. Hoffman, and S. C. Vogel, *Mech. Mater.* **39**, 283 (2007).
49 D. A. Hall, A. Steuwer, B. Cherdhirunkorn, T. Mori, and P. J. Withers, *Acta Mater.* **54**,
50 3075 (2006).
51 D. A. Hall, A. Steuwer, B. Cherdhirunkorn, P. J. Withers, and T. Mori, *J. Mech. Phys.*
52 *Solids* **53**, 249 (2005).
53 D. J. Franzbach, B.-X. Xu, R. Mueller, and K. G. Webber, *Appl. Phys. Lett.* **99**, 162903
54 (2011).
55 F. Jona and G. Shirane, *Ferroelectric Crystals* (Pergamon Press, New York, 1962).
56 A. F. Devonshire, *Philos. Mag.* **40**, 1040 (1949).
57 L. Q. Chen, *Annu. Rev. Mater. Sci. Res.* **32**, 113 (2002).
58 J. J. Wang, P. P. Wu, X. Q. Ma, and L. Q. Chen, *J Appl. Phys.* **108**, 114105 (2010).
59 M. J. Haun, Z. Q. Zhuang, E. Furman, S. J. Jang, and L. E. Cross, *Ferroelectrics* **99**, 45
60 (1989).
61 T. Yamada, *J. Appl. Phys.* **43**, 328 (1972).
62 G. A. Rossetti Jr., L. E. Cross, and K. Kushida, *Appl. Phys. Lett.* **59**, 2524 (1991).
63 G. A. Samara, *Phys. Rev.* **151**, 378 (1966).
64 J. Frantti, S. Ivanov, S. Eriksson, H. Rundlöf, V. Lantto, J. Lappalainen, and M.
65 Kakihana, *Phys Rev B* **66**, 064108 (2002).
66 A. F. Devonshire, *Phil. Mag.* **42**, 1065 (1951).
67 V. Sundar and R. E. Newnham, *Ferroelec.* **135**, 431 (1992).
68 H. Goldstein, *Classical Mechanics* (Addison-Wesley Pub. Co., Reading, MA, 1980).
69 D. Vanderbilt and M. H. Cohen, *Phys. Rev. B* **63** (2001).
70 D. Damjanovic and M. Demartin, *J. Phys.: Condens. Matter* **9**, 4943 (1997).